ATLAS NOTE

ATLAS-CONF-2011-147

October 17, 2011

Searches for TeV-gravity signatures in final states with leptons and jets with the ATLAS detector at $\sqrt{s} = 7$ TeV

The ATLAS Collaboration

Abstract

The production of high transverse momentum events containing charged leptons and jets has been measured, using 1.04 fb^{-1} of data recorded by the ATLAS detector in 2011 at $\sqrt{s}$ = 7 TeV. No excess beyond Standard Model expectations is observed, and upper limits on effective cross sections are set. Using models for string ball and black hole production and decay, exclusion contours are determined as a function of mass threshold and the fundamental gravity scale.

1 Introduction

Low-scale gravity models allow the existence of non-perturbative gravitational states such as black holes and, within the context of weakly-coupled string theory, string balls. Were such a new physics scale to be in the TeV range, the exploration of these states would be feasible at the Large Hadron Collider (LHC).

Models proposing extra spatial dimensions can provide solutions to the hierarchy problem in which the gravitational field propagates into the $(n + 4)$ dimensions, where n is the number of extra spatial dimensions, whilst Standard Model (SM) fields are constrained to lie in our $(3 + 1)$-dimensional brane. Consequently, the observed gravitational field is weakened with respect to the fundamental gravitational field strength. The resulting Planck scale in $(n + 4)$ dimensions, M_{D}, is greatly diminished compared to the 4-dimensional analogue, M_{Pl}, and should be near the other fundamental scale, the electroweak scale, as a solution to the hierarchy problem. Two particularly interesting extra-dimension scenarios, which could provide similar TeV-scale gravitational interaction signatures at the LHC, are the "warped" models [1] and the large, compactified extra dimensional models [2, 3]. In the original warped scenario, there is a single warped extra dimension ($n = 1$) which separates two 3-dimensional branes by some distance. Gravitons can propagate in this warped dimension and the effective Planck scale on the 3-dimensional brane where the Standard Model fields reside is determined by the curvature of the extra dimension, also referred to as the warp factor. In the large extra dimension scenario, there are a number $n > 1$ of additional flat extra dimensions, and M_{D} is determined by the volume and shape of the extra dimensions. Within the context of this model, experimental lower limits on the value of M_{D} have been obtained from experiments at LEP [4] and the Tevatron [5, 6], as well as at ATLAS [7] and CMS [8], by searching for production of the heavy Kaluza-Klein gravitons associated with the extra dimensions. The most stringent limits [7] come from the LHC analyses that search for non-interacting gravitons recoiling against a single jet (monojet and large missing transverse energy), and range from $M_{\mathrm{D}} > 2.0$ TeV, for $n = 6$, to $M_{\mathrm{D}} > 3.2$ TeV, for $n = 2$. Due to the greatly enhanced strength of gravitational interactions at short distances, or high energies, the formation of non-perturbative gravitational states such as black holes or string balls at the LHC is another signature of extra dimensional models.

Although inspired by string theory, the large extra dimensional paradigm is not based on it. However, embedding large extra dimensions into weakly-coupled string theory could provide an understanding of the strong-gravity regime and the picture of the evolution of a black hole at the last stages of evaporation [9, 10]. In this picture, black holes end their Hawking evaporation when their mass reaches a critical mass M_{S}. At this point they transform into high-entropy string states – string balls – without ever reaching the singular zero-mass limit.

Both the large extra dimension and warped models of black holes (and string balls) assume classical general relativity for their production and semi-classical Hawking evaporation for the decays, resulting in final states distinguished by a high multiplicity of high-p_{T} particles. Black hole production at a particle collider is assumed to occur with a continuous mass distribution ranging from a mass threshold, M_{TH}, somewhere above M_{D}, up to the proton-proton collision energy, $\sqrt{s}$. Semi-classical approximations used in the modelling are valid only well above M_{D}, motivating the use of a minimal threshold M_{TH} to remove contributions where the modelling is not reliable. The precise mass value ($M_{\mathrm{TH}} > M_{\mathrm{D}}$), above which the production of such high multiplicity states is feasible is uncertain. A conservative interpretation [11, 12] is that $M_{\mathrm{TH}} > 3M_{\mathrm{S}}$ for string balls and $M_{\mathrm{TH}} > 5M_{\mathrm{D}}$ for black holes, where M_{S} is the string scale in weakly-coupled string theory. Theoretical predictions for black hole production cross sections usually assume that all incoming parton centre-of-mass energy forms the black hole, which forms when half the

impact parameter of the colliding partons is less than the higher-dimensional radius for a black hole of mass equal to this energy [13].

Thermal radiation is thought to be emitted by black holes due to quantum effects [14]. A black hole of given mass and angular momentum (in n extra dimensions) is characterised by a Hawking temperature, which is higher for a lighter, or more strongly rotating, black hole. Grey-body factors modify the spectrum of emitted particles from that of a perfect thermal black body [15], by quantifying the transmission probability through the curved space-time outside the horizon. All Standard Model particles are emitted, with relative emissivities that are dependent upon their number of degrees of freedom, spin, n and the properties of the black hole. Baryon and lepton number do not have to be conserved in black hole decay.

If black hole or string ball states are produced at the LHC then they will decay to final states with a relatively high multiplicity of high-p_{T} particles, most commonly jets. Though generally high, the exact multiplicity spectrum is rather model dependent: for example, the inclusion of black hole rotation leads to a rather lower multiplicity of higher energy emissions [16]. One of the few relatively robust predictions of these models is the expectation that particles are produced approximately according to the Standard Model degrees of freedom and are not affected by the strengths of the forces described by the Standard Model. This is the "democratic" or "universal" coupling of gravity. Hence, these models predict the existence of at least one high-p_{T} lepton[1] in a significant fraction ($\sim 15-50$ %) of final states for black holes or string balls with M_{D} and M_{TH} values in the range accessible to LHC experiments and not already excluded. The largest theoretical uncertainties in the modelling of these states are the limited knowledge of gravitational radiation and the resultant cross section during the formation phase, and the uncertainties of the decay process as the black hole mass approaches the M_D, (the treatment of the remnant state).

Searches for these states have previously been performed by investigating final states with multiple high-p_{T} objects [17, 18, 19], high-p_{T} jets only [20], and in dimuon events [21]. This analysis searches for an excess of multi-object events produced at high $\sum p_{\mathrm{T}}$, defined as the sum of p_{T} of the reconstructed objects considered in this note (hadronic jets, electrons and muons). Only events containing at least one isolated electron or muon are selected. While jets should dominate the decays of black holes[2], the rate for lepton production is anticipated to be sizable, as noted above, and the requirement of a high-p_{T} lepton significantly reduces the dominant QCD multi-jet background, of which our knowledge of the production at LHC energies is limited, whilst maintaining a high efficiency for black hole events.

The method presented here is not sensitive to two-body final states. If the process is such that a black hole decays to only two bodies, as in so-called quantum black hole states [22] (characterised as having masses near M_{D}, the mass scale of quantum gravity), a dedicated two-body search is the best way to rule out this scenario [23]. Therefore this search considers final states with three or more objects, including electrons, muons, and jets amongst the selected objects.

2 The ATLAS Detector

The ATLAS detector [24] is a multipurpose particle physics apparatus with a forward-backward symmetric cylindrical geometry and nearly 4π coverage in solid angle[3]. The layout of the detector is dominated

[1] Throughout this note "lepton" denotes electrons and muons only.

[2] In this note, when referring to black holes, we are also referring to string balls, unless otherwise stated.

[3] ATLAS uses a right-handed coordinate system with its origin at the nominal interaction point in the centre of the detector and the z-axis along the beam pipe. Cylindrical coordinates (r, ϕ) are used in the transverse plane, ϕ being the azimuthal angle around the beam pipe. The pseudorapidity η is defined in terms of the polar angle θ by $\eta = -\ln\tan(\theta/2)$.

by four superconducting magnet systems, which comprise a thin solenoid surrounding inner tracking detectors and three large toroids supporting a large muon tracker. The inner detector consists of a silicon pixel detector, a silicon microstrip detector (SCT) and a transition radiation tracker (TRT). In the pseudorapidity region $|\eta| < 3.2$, high-granularity liquid-argon (LAr) electromagnetic (EM) sampling calorimeters are used. An iron-scintillator tile calorimeter provides hadronic coverage over $|\eta| < 1.7$. The end-cap and forward regions, spanning $1.5 < |\eta| < 4.9$, are instrumented with LAr calorimetry for both EM and hadronic measurements. The muon spectrometer surrounds these, and comprises a system of precision tracking chambers, and detectors for triggering.

3 Trigger and Data Selection

The data used in this analysis were recorded between March and July 2011, with the LHC operating at a centre-of-mass energy of 7 TeV. Application of detector data-quality requirements gives a total integrated luminosity of 1.04 fb^{-1}, with an uncertainty of 3.7% [25].

Events are required to pass either a single electron or a single muon trigger, for the electron and muon channels respectively. The p_{T} thresholds of these triggers are 20 GeV and 18 GeV for the electron and muon triggers respectively. The trigger efficiency turn-on curves reach the plateau region for electrons and muons at transverse momenta values substantially below the minimum threshold used in this analysis of 40 GeV, with typical trigger efficiencies for leptons selected for offline analysis of: 96% for electrons [26], 75% for muons with $|\eta| < 1.05$ and 88% for muons with $1.05 < |\eta| < 2.0$ [27]. To assure good data quality, only runs for which all ATLAS subdetectors are preforming well are used.

4 Monte Carlo Samples

Monte Carlo (MC) simulated event samples are used to develop and validate the analysis procedure, to help estimate the SM backgrounds in the signal region and to investigate specific signal models. Samples of QCD jet events are generated with `Pythia` [28], using the `MRST2007LO*` modified leading-order parton distribution functions (PDF) [29], which are used with all leading-order (LO) Monte Carlo generators. Production of top quark pairs is simulated with `MC@NLO` [30] (with a top quark mass of 172.5 GeV) and the next-to-leading order (NLO) PDF set `CTEQ6.6` [31], which is used with all NLO MC generators. Samples of W and Z/γ^* Monte Carlo events with accompanying jets are produced with `Alpgen` [32], using the `CTEQ6L1` PDFs [33], and events generated with `Sherpa` [34] are used to assess the systematic uncertainty associated with choice of MC generator. Diboson (WW, WZ, ZZ) production is simulated with `Herwig` [35] and single top-quark production with `MC@NLO` [30]. Fragmentation and hadronisation for the `Alpgen` and `MC@NLO` samples are performed with `Herwig`, using `Jimmy` [36] for the underlying event. All MC samples are produced using a specific ATLAS parameter tune [37] and the ATLAS full GEANT4 [38] detector simulation [39].

Signal samples are generated with the `Charybdis` [16] and `Blackmax` [40, 41] generators. The shower evolution and hadronisation uses `Pythia`, with the `CTEQ6.6` PDF sets using the black hole mass as the QCD scale. No radiation losses in the formation phase are modelled. The `Charybdis` samples are generated with both low and high multiplicity remnants, whilst the `Blackmax` samples use the final burst remnant model, which gives high multiplicity remnant states [40]. Samples are generated for both rotating and non-rotating black holes for six extra dimensions. Focus is placed on models with six extra dimensions due to the less stringent limits on M_{D}. String ball samples are produced with `Charybdis` for both rotating and non-rotating cases, for six extra dimensions, and a string coupling, g_{S}, of 0.4. Two

Charybdis samples with six extra dimensions are used to guide the analysis and illustrate the potential signal properties: a non-rotating black hole sample with $M_{TH} = 4.0$ TeV and $M_D = 0.8$ TeV, and a rotating stringball sample with a 3 TeV threshold and $M_S = 1.0$ TeV.

A set of benchmark samples are produced, for rotating black holes and for rotating and non-rotating string balls (using Charybdis with a high multiplicity remnant state), with M_D ranging between 0.5 and 2.5 TeV, and M_{TH} varying from 2 TeV to 5 TeV. Two rotating black hole sample sets are generated, with Hawking evaporation phases terminated by differing remnant models: one with a high multiplicity remnant state, generated using Blackmax and another using a low multiplicity (two-body) remnant state, produced using Charybdis. These samples are used in setting exclusion contours in the M_D-M_{TH} plane.

5 Object Reconstruction

Electrons are reconstructed from clusters in the electromagnetic calorimeter matched to a track in the inner detector [42]. A set of electron identification criteria based on the calorimeter shower shape and track quality and track matching with the calorimeter cluster are described in Ref. [42] and are referred to as 'loose', 'medium' and 'tight'. Preselected electrons are required to have $p_T > 40$ GeV, $|\eta| < 2.47$ and to pass the 'medium' electron definition. Electron candidates are required to be isolated: the sum of the transverse energy deposited within a cone of $\Delta R < 0.2$ around the electron candidate (excluding the electron candidate itself, and corrected for transverse shower leakage and pile-up from additional pp collisions) is required to be less than 10% of the electron p_T. Electrons with a distance to the closest jet of $0.2 < \Delta R < 0.4$ are discarded, where $\Delta R = \sqrt{(\Delta\eta)^2 + (\Delta\phi)^2}$. For electrons in the signal region, the quality criterion is raised to 'tight'.

Preselected muons are the result of a combined track in the muon spectrometer and in the inner detector. Muons are required to have $p_T > 40$ GeV. Muon candidates are required to have an associated inner detector track with sufficient hits in the pixel, SCT and TRT detectors to ensure a good measurement. Additional requirements are made on the muon system hits in order to guarantee the best possible resolution at high p_T: muon candidates must have hits in at least three precision layers and no hits in detector regions with limited alignment precision. These requirements effectively restrict the muon acceptance to the barrel region ($|\eta| < 1.0$) and a portion of the end-cap region ($1.3 < |\eta| < 2.0$) [43]. Muons with a distance to the closest jet of $\Delta R < 0.4$ are discarded. In order to reject muons resulting from cosmic rays, tight cuts are applied to the origin of the muons relative to the primary vertex (PV) ($|z_0| = |z_\mu - z_{PV}| < 1$ mm and $|d_0| < 0.2$ mm, where z_0 and d_0 are the impact parameters of each muon in the longitudinal and transverse planes, respectively). Muons must be isolated: the p_T sum of tracks within a cone of $\Delta R < 0.3$ around the muon candidate (excluding the muon candidate itself) is required to be less than 5% of the muon p_T.

Jets are reconstructed using the anti-k_t jet clustering algorithm [44] with a radius parameter of 0.4. The inputs to the jet algorithm are clusters seeded from calorimeter cells with energy deposits significantly above the measured noise [45]. Jets are corrected for effects from calorimeter non-compensation and inhomogeneities through the use of p_T- and η-dependent calibration factors based on Monte Carlo corrections validated with test-beam and collision data [46]. This calibration corresponds to the scale that would be obtained applying the jet algorithm to stable particles at the primary collision vertex. Preselected jets are required to have $p_T > 40$ GeV and $|\eta| < 2.8$. Events with jets failing jet quality criteria against noise and non-collision backgrounds [47] are rejected. Jets within a distance $\Delta R < 0.2$ of a preselected electron are also rejected.

The missing transverse momentum $E_{\mathrm{T}}^{\mathrm{miss}}$ in this analysis is the opposite of the vectorial p_{T} sum of reconstructed objects in the event, comprising jets with $p_{\mathrm{T}} > 20$ GeV, leptons selected according to the description above, any additional identified non-isolated muons, and calorimeter clusters not belonging to any of the aforementioned object types. $E_{\mathrm{T}}^{\mathrm{miss}}$ is not considered as an object in this analysis, nor included in $\sum p_{\mathrm{T}}$, primarily due to the large uncertainties on its modelling in the Monte Carlo signal event generators, and is used solely in the definitions of regions for background estimation.

Photons and hadronically-decaying tau leptons are not explicitly identified in this analysis, and are reconstructed as jets.

6 Event Selection

Events are required to have a reconstructed primary vertex associated with at least five tracks. During the data-taking period considered, an electronic failure in the LAr barrel calorimeter resulted in a small "dead" region, in which up to 30% of the incident jet energy may be lost. Should any of the four leading jets with $p_{\mathrm{T}} > 40$ GeV fall into this region, the event is vetoed. This is applied to all data and Monte Carlo events, and results in a loss of signal efficiency of $\sim 15 - 20\%$ for the models considered. Additionally, electrons incident on this region are removed. Selected events contain at least one high-p_{T} (> 40 GeV) isolated lepton. Two statistically independent samples are defined by separating events for which the leading lepton (that of highest p_{T}) is an electron (muon) into an *electron* (*muon*) channel sample. The corresponding single lepton trigger is required to have fired.

High multiplicity final states of interest can be separated effectively from Standard Model background events using the quantity:

$$\sum p_{\mathrm{T}} = \sum_{i=\mathrm{objects}} p_{\mathrm{T},i}\,, \tag{1}$$

which is the scalar sum of the transverse momenta of selected final state reconstructed objects (leptons and jets), described in Section 5. The signal, containing multiple high-p_{T} objects, manifests itself at high $\sum p_{\mathrm{T}}$.

Preselection requirements are used to select a sample of events with similar kinematics and composition to the signal regions for this search. Events are required to have at least three objects passing the 40 GeV p_{T} threshold and have a moderate $\sum p_{\mathrm{T}} > 300$ GeV. Additionally, the electron channel requires an electron to pass the 'tight' selection. Control regions (CR), used to evaluate the backgrounds using data-driven methods, consider subsets of events passing these preselection requirements. Figure 1 shows the transverse momentum of the leading lepton after event preselection requirements for electron and muon channels, where the background distributions have been normalised to be in agreement with data in selected control regions, as described in Section 7.

For the signal region (SR), the $\sum p_{\mathrm{T}}$ and object p_T cuts are raised further. Events are required to contain at least three reconstructed objects with $p_{\mathrm{T}} > 100$ GeV, at least one of which must be a lepton. These events are required to have a minimum $\sum p_{\mathrm{T}}$ of 700 GeV. To determine limits on the effective cross section, this threshold is varied between 700 and 1500 GeV. In making exclusion contours in the M_{D}-M_{TH} plane, using the benchmark models described in Section 4, a single signal region is used, defined by a $\sum p_{\mathrm{T}} > 1500$ GeV requirement.

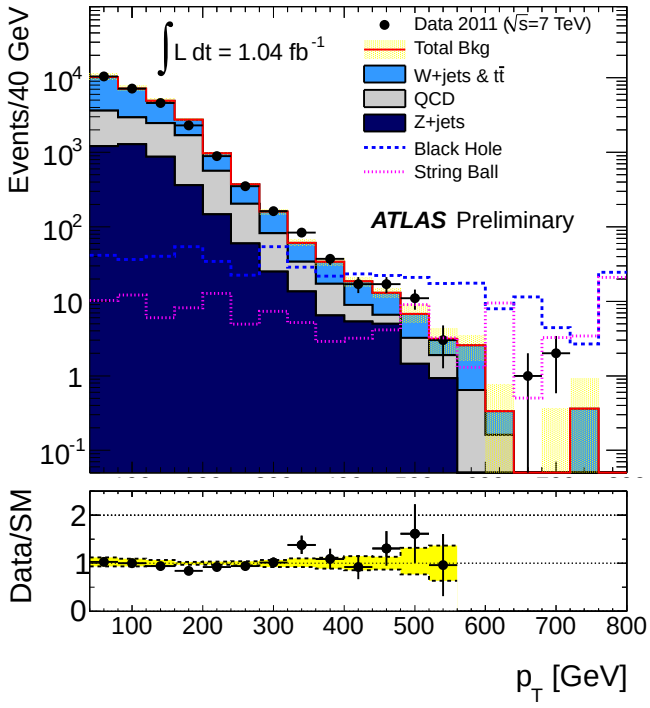

(a) Transverse momentum of leading electron.

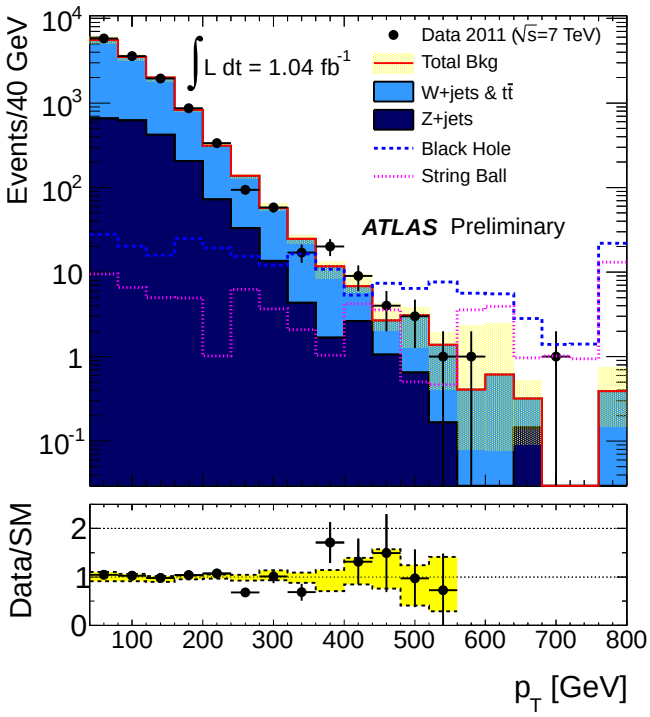

(b) Transverse momentum of leading muon.

Figure 1: Transverse momentum of the highest momentum lepton, after preselection. The Monte Carlo distributions are rescaled to be in agreement with data in selected control regions, as described in Section 7. The yellow band indicates the uncertainty on the expectation from finite statistics, jet and lepton energy scales and resolutions. Two representative signal distributions are overlaid for comparison purposes. The signal labelled "Black Hole" is a non-rotating black hole sample with $n = 6$, $M_D = 0.8$ TeV and $M_{TH} = 4$ TeV. The signal labelled "Stringball" is a rotating string ball sample with $n = 6$, $M_D = 1.26$ TeV, $M_S = 1$ TeV and $M_{TH} = 3$ TeV. Both signal samples were generated with the `Charybdis` generator. The last bin in the signal sample histograms is the integral of all events with $p_T \geq 760$ GeV.

7 Background Estimation

The backgrounds are estimated using a combination of data-driven and MC-based techniques. The dominant Standard Model sources of background are: W+jets, Z/γ^*+jets, $t\bar{t}$ and other QCD multi-jet processes. In QCD events, one jet fakes a high-p_{T} lepton. In W+jets, Z/γ^*+jets and $t\bar{t}$ events, events are produced with prompt leptons, and associated additional high-p_{T} jets.

The contribution to the muon channel signal region from QCD multi-jets is predicted by MC simulations to be negligible. This has been cross-checked by estimating in data the contribution using a sample of events containing non-isolated muons, dominated by QCD multi-jet processes, and extrapolating the result to the signal selection criteria.

The QCD multi-jet contribution to the electron channel is estimated using a data-driven matrix method, described in detail in Ref. [48]. Using the signal region definition, a QCD multi-jet enhanced region is defined by loosening the electron identification criterion used in the event selection from 'tight' to 'medium'. The numbers of data events in this "looser" electron sample which pass (N_{pass}) and fail (N_{fail}) the final, tighter lepton selection criteria are counted. N_{real} and N_{fake} are defined as the numbers of events for which the electrons are real and fake, respectively. The following relationships hold:

$$N_{\mathrm{pass}} = \epsilon_{\mathrm{real}} N_{\mathrm{real}} + \epsilon_{\mathrm{fake}} N_{\mathrm{fake}}, \tag{2}$$

$$N_{\mathrm{fail}} = (1 - \epsilon_{\mathrm{real}}) N_{\mathrm{real}} + (1 - \epsilon_{\mathrm{fake}}) N_{\mathrm{fake}}. \tag{3}$$

Simultaneous solution of these two equations gives a prediction for the number of events in data in the signal region which are events with fake leptons:

$$N_{\mathrm{fake}}^{\mathrm{pass}} = \epsilon_{\mathrm{fake}} N_{\mathrm{fake}} = \frac{N_{\mathrm{fail}} - (1/\epsilon_{\mathrm{real}} - 1) N_{\mathrm{pass}}}{1/\epsilon_{\mathrm{fake}} - 1/\epsilon_{\mathrm{real}}} \tag{4}$$

The efficiency ϵ_{fake} is determined from a data control region defined by $300 < \sum p_{\mathrm{T}} < 700$ GeV and $E_{\mathrm{T}}^{\mathrm{miss}} < 15$ GeV, in which events must have a least three reconstructed objects passing preselection criteria, with at least one preselected electron. QCD multi-jet dominated samples are obtained by loosening the electron identification criteria used in the event preselection from 'tight' to 'medium'. The efficiency for misidentifying fake electrons is measured for these events by considering the fraction which pass the tighter electron identification requirement. According to MC simulation, the contribution from QCD processes to this sample is $\sim 85\%$. The efficiency is corrected to account for the small fraction of prompt, real electrons, using the prediction from MC simulations. The dependence of ϵ_{fake} on lepton p_T and $\sum p_{\mathrm{T}}$ is considered.

The efficiency ϵ_{real} is evaluated in a second control region, again containing at least three reconstructed objects, but with at least two opposite-sign electrons satisfying $80 < m_{\ell\ell} < 100$ GeV (*i.e.* electron pairs with invariant mass near the Z mass). The efficiency for identifying real, prompt electrons is obtained through the ratio of "medium-medium" to "medium-tight" events. The MC simulation predicts that more than 99% of the electron candidates in this control region are real, prompt electrons.

The numbers of Z/γ^*+jets events in the SR for each channel are estimated by measuring the ratio of the number of events in data to the number of events in MC simulation in a control region with: two opposite-sign leptons (two electrons or two muons) with $80 < m_{\ell\ell} < 100$ GeV, at least three preselected objects, and $300 < \sum p_{\mathrm{T}} < 700$ GeV. This ratio is a scaling factor (SF) that is then used to rescale the

pure MC prediction in the signal region. These scaling factors are found to be $SF = 0.85 \pm 0.04 \pm 0.14$ and $SF = 0.93 \pm 0.03 \pm 0.08$, for muons and electrons, respectively, where the first errors are statistical and the second are systematic.

The number of W+jets and $t\bar{t}$ events in the SR is estimated in a similar fashion, by defining a control region containing events with: exactly one electron (or muon, separately) with $40 < M_{\mathrm{T}} < 100$ GeV, where M_{T} is the "transverse W mass" calculated from the components of the lepton momentum transverse to the beam direction and the missing transverse momentum vector; $30 < E_{\mathrm{T}}^{\mathrm{miss}} < 60$ GeV, at least three objects; and $300 < \sum p_{\mathrm{T}} < 700$ GeV. Due to their similar behaviour in $\sum p_{\mathrm{T}}$, W+jets and $t\bar{t}$ events are treated as a single background; a scaling factor is derived and used to rescale the pure MC prediction in the signal region. These scaling factors are found to be $SF = 1.05 \pm 0.02 \pm 0.12$ and $SF = 0.93 \pm 0.02 \pm 0.14$, for muons and electrons, respectively, where the first errors are statistical and the second are systematic.

8 Systematic Uncertainties

In this analysis, the dominant sources of systematic uncertainty on the estimated background event rates are: choice of the control regions used to derive the background estimates (for the QCD and Z+jets backgrounds), MC modelling uncertainties assessed using alternative samples produced with different generators (for the Z+jet, W+jet and $t\bar{t}$ backgrounds) and the calibration of the jet energy scale (JES). Other uncertainties include the jet energy resolution uncertainty (JER), uncertainties in lepton reconstruction and identification (momentum scales, resolutions and reconstruction efficiencies), PDF uncertainties and the uncertainties in the effects of initial and final-state radiation. For the Z+jets, W+jets and $t\bar{t}$ backgrounds the use of a CR region in data to renormalise the MC predictions, as described in Section 7, mitigates the effects of most of the systematic uncertainties, which act primarily to vary the overall magnitude of the predicted backgrounds. The residual systematic uncertainty in the signal region is due to alterations of the shapes of the $\sum p_{\mathrm{T}}$ distributions. For the background estimates of Z+jet, W+jet and $t\bar{t}$ processes, the dominant uncertainties are those associated with the extrapolation of the background shape to the signal region, followed by the calibration of the jet energy scale. The sizes of the systematic uncertainties described above vary, depending on the channel and on the $\sum p_{\mathrm{T}}$ range of the SR, but are typically $15 - 20\%$, except for the highest $\sum p_{\mathrm{T}}$ bins for which the MC statistics are small and larger fluctuations are observed.

The JES and JER uncertainties are applied to Monte Carlo simulated jets, and are propagated throughout the analysis to assess their effect. The JES uncertainties applied are those measured using the complete 2010 dataset using the techniques described in Ref. [46]. The JER measured with 2010 data [49] is applied to all Monte Carlo simulated jets, with the difference between the nominal and recalibrated values taken as the systematic uncertainty. Additional contributions are added to both of these uncertainties to account for the effect of high luminosity pile-up in the 2011 run. The effect of in-time pile-up on other analysis-level distributions was investigated and found to be negligible, as is expected in light of the high-p_{T} objects populating the signal region.

9 Results

The observed and predicted event yields, following the estimations described in Section 7, are given in Tables 1 and 2, as a function of minimum $\sum p_{\mathrm{T}}$. The agreement between the data and the background model expectation is good, and the distribution of $\sum p_{\mathrm{T}}$ is shown in Figure 2. The distribution of p_{T} of

the object with the highest value of p_{T} is shown in Figure 3. No evidence of a signal is observed, with SM background estimates in good agreement with the observed data, for all choices of $\sum p_{\mathrm{T}}$ threshold.

$\sum p_{\mathrm{T}}$ (GeV)	QCD	W+jets/$t\bar{t}$	Z+jets	Total SM	Data
> 700	$137 \pm 10 \pm 45$	$371 \pm 10 \pm 77$	$119 \pm 4 \pm 22$	$627 \pm 15 \pm 92$	586
> 800	$75 \pm 7 \pm 25$	$210 \pm 6 \pm 42$	$74 \pm 4 \pm 13$	$358 \pm 10 \pm 51$	348
> 900	$42 \pm 5 \pm 14$	$122 \pm 5 \pm 28$	$46.9 \pm 2.8 \pm 8.6$	$210 \pm 8 \pm 33$	196
> 1000	$24.6 \pm 4.2 \pm 8.0$	$73 \pm 3 \pm 17$	$22.2 \pm 1.8 \pm 4.5$	$119 \pm 5 \pm 20$	113
> 1200	$8.1 \pm 2.5 \pm 2.7$	$28.5 \pm 1.8 \pm 7.6$	$9.1 \pm 1.0 \pm 1.9$	$45.7 \pm 3.2 \pm 8.3$	41
> 1500	$1.3 \pm 1.1 \pm 0.4$	$6.3 \pm 0.8 \pm 2.5$	$2.6 \pm 0.5 \pm 0.5$	$10.2 \pm 1.4 \pm 2.6$	8

Table 1: Background estimation summary as a function of $\sum p_{\mathrm{T}}$ in the electron channel, using the methods described in the main body of this note. The first quoted errors are statistical, the second systematic. All other backgrounds considered (WW, ZZ and WZ) are estimated to have negligible contributions.

$\sum p_{\mathrm{T}}$ (GeV)	W+jets/$t\bar{t}$	Z+jets	Total SM	Data
> 700	$236 \pm 7 \pm 43$	$49 \pm 3 \pm 11$	$285 \pm 8 \pm 44$	241
> 800	$129 \pm 4 \pm 25$	$32.0 \pm 2.4 \pm 7.5$	$161 \pm 5 \pm 26$	145
> 900	$71 \pm 3 \pm 16$	$19.5 \pm 1.7 \pm 5.0$	$91 \pm 3 \pm 16$	78
> 1000	$38.9 \pm 2.3 \pm 8.3$	$13.1 \pm 1.3 \pm 3.1$	$52.0 \pm 2.6 \pm 8.9$	46
> 1200	$9.9 \pm 1.2 \pm 3.6$	$4.0 \pm 0.6 \pm 1.2$	$14.0 \pm 1.3 \pm 3.8$	15
> 1500	$2.2 \pm 0.5 \pm 1.1$	$0.6 \pm 0.2 \pm 0.4$	$2.8 \pm 0.5 \pm 1.1$	2

Table 2: Background estimation summary as a function of $\sum p_{\mathrm{T}}$ in the muon channel, using the methods described in the main body of this note. The first quoted errors are statistical, the second systematic. All other backgrounds considered (WW, ZZ, WZ and QCD multi-jet processes) are estimated to have negligible contributions.

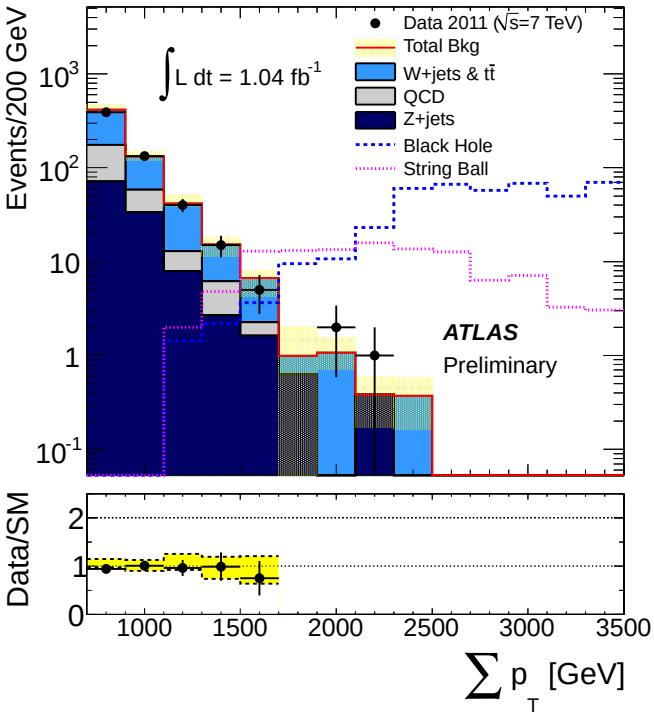

(a) Electron channel

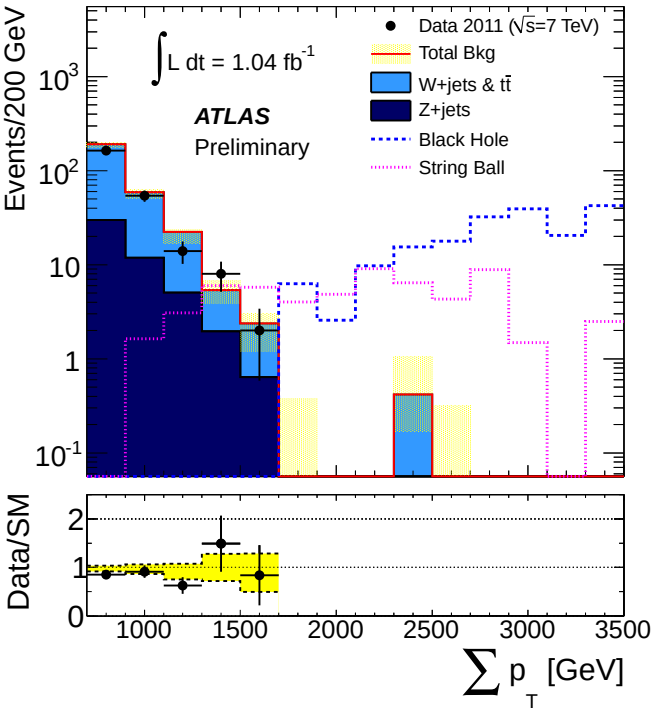

(b) Muon channel

Figure 2: Final $\sum p_{\mathrm{T}}$ distributions for the signal region. Background processes are shown according to their data-derived estimates, as described in the text. The yellow band indicates the uncertainty on the expectation from finite statistics, jet and lepton energy scales and resolutions. Two representative signal distributions are overlaid for comparison purposes. The signal labelled "Black Hole" is a non-rotating black hole sample with $n = 6$, $M_{\mathrm{D}} = 0.8$ TeV and $M_{\mathrm{TH}} = 4$ TeV. The signal labelled "Stringball" is a rotating string ball sample with $n = 6$, $M_{\mathrm{D}} = 1.26$ TeV, $M_{\mathrm{S}} = 1$ TeV and $M_{\mathrm{TH}} = 3$ TeV. The last bin in the signal sample histograms is the integral of all events with $\sum p_{\mathrm{T}} \geq 3300$ GeV.

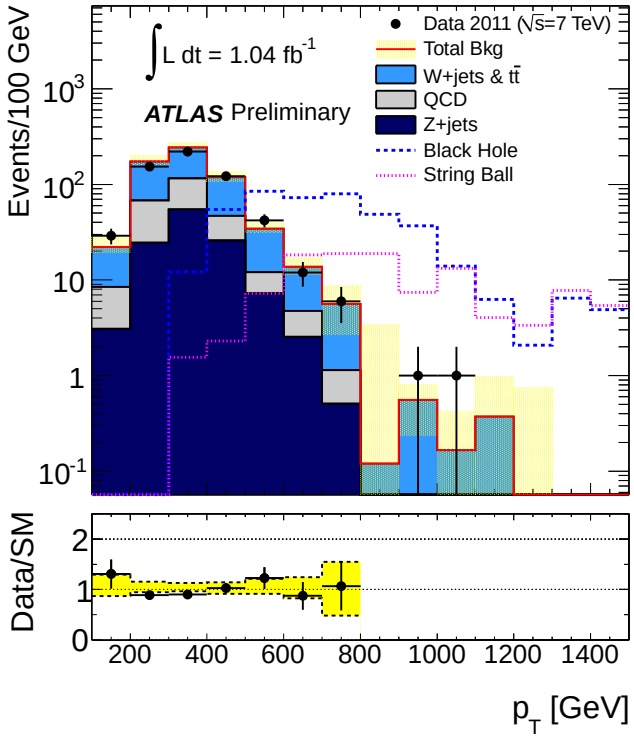

(a) Electron channel

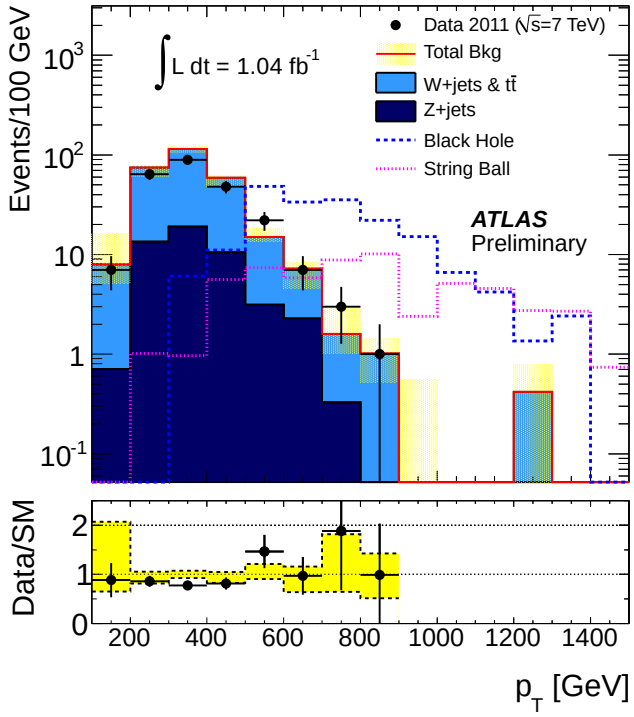

(b) Muon channel

Figure 3: Final distributions for p_{T} of the object (jet or lepton) with the largest value of p_{T} for the signal region. Background processes are shown according to their data-derived estimates, as described in the text. The yellow band indicates the uncertainty on the expectation from finite statistics, jet and lepton energy scales and resolutions. Two representative signal distributions are overlaid for comparison purposes. The signal labelled "Black Hole" is a non-rotating black hole sample with $n = 6$, $M_{\mathrm{D}} = 0.8$ TeV and $M_{\mathrm{TH}} = 4$ TeV. The signal labelled "Stringball" is a rotating string ball sample with $n = 6$, $M_{\mathrm{D}} = 1.26$ TeV, $M_{\mathrm{S}} = 1$ TeV and $M_{\mathrm{TH}} = 3$ TeV. The last bin in the signal sample histograms is the integral of all events with $p_{\mathrm{T}} \geq 1400$ GeV.

10 Interpretation

No excess is observed beyond the Standard Model expectation; *p-values* for the signal regions are in the range 0.43 – 0.47. Therefore, model-independent exclusion limits are determined on the effective cross section, σ_{eff}, for new physics that results in these final states as a function of minimum $\sum p_{\text{T}}$. The effective cross section is defined as: $\sigma_{\text{eff}} = \sigma(pp \to \ell X) \cdot \epsilon_{\text{rec}} \cdot \epsilon_{\text{acc}}$, where $\sigma(pp \to \ell X)$ is the production cross section for a high-$\sum p_{\text{T}}$ multi-object state containing a high-p_{T} (> 100 GeV) isolated lepton inside experimental acceptance. For the models considered $\epsilon_{\text{rec}} \cdot \epsilon_{\text{acc}}$ varies; its average values are 74% for the electron channel and 51% for the muon channel. The full range of $\epsilon_{\text{rec}} \cdot \epsilon_{\text{acc}}$ is 60 – 90% for the electron channel and 40 – 60% for the muon channel. The acceptance for the muon channel is lower than that for the electron channel because of the lower trigger efficiency (Section 3) and the more stringent requirements (Section 5) needed to guarantee the best possible resolution at high p_{T}. For the models considered, the total signal acceptance is highly model-dependent, driven primarily by the fraction of events containing a lepton in the final states, and averages about 10% and 5% for the (mutually exclusive) electron and muon channels respectively. It is lowest for the low multiplicity, low mass states (small values of $M_{\text{TH}}/M_{\text{D}}$, or M_{TH} and M_{D}) that are theoretically or experimentally disfavoured.

The observed and expected event counts and their uncertainties are used to set limits on the allowed effective cross section for black hole production, as a function of $\sum p_{\text{T}}$ threshold. These exclusion regions are obtained using the CL_{s} prescription [50], and are shown in Figure 4. The 95% confidence level (C.L.) upper limits on the cross section are summarised in Table 3. A similar search [19] performed by the CMS collaboration, also using a data sample corresponding to an integrated luminosity of ~ 1 fb^{-1}, found upper limits of about 3 fb, for the highest values of $\sum p_{\text{T}} + E_{\text{T}}^{\text{miss}}$ (> 3.5 TeV), but for an inclusive multi-object final state (without a lepton requirement).

$\sum p_{\text{T}}$ (GeV)	σ_{eff} 95% C.L. Upper Limit (fb) Observed (Expected)	
	Muon Channel	Electron Channel
> 700	77 (94)	169 (188)
> 800	51 (58)	102 (112)
> 900	32 (39)	65 (73)
> 1000	20 (24)	43 (45)
> 1200	13 (12)	20 (22)
> 1500	4.8 (4.8)	8.7 (9.7)

Table 3: Upper limits on the effective cross sections ($\sigma_{\text{eff}} = \sigma(pp \to \ell X) \cdot \epsilon_{\text{rec}} \cdot \epsilon_{\text{acc}}$) for black hole production, at the 95% C.L., for muon and electron channels. For the models considered, $\epsilon_{\text{rec}} \cdot \epsilon_{\text{acc}}$ varies, averaging 74% (51%) for the electron (muon) channel. The full range of $\epsilon_{\text{rec}} \cdot \epsilon_{\text{acc}}$ is 60 – 90% for the electron channel and 40 – 60% for the muon channel. The CL_{s} method is used to obtain the limits.

The observed counts of data events in the signal region (for $\sum p_{\text{T}} > 1500$ GeV) along with the background expectations are used to obtain exclusion contours in the plane of M_{D} and M_{TH} for several benchmark models (rotating and non-rotating black holes or string balls) that are considered representative of the gravitational states to which this analysis has sensitivity. No theoretical uncertainty on signal prediction is assessed; that is, the exclusion limits are set for the exact benchmark models as implemented in the `Blackmax` and `Charybdis` generators. Experimental systematic and luminosity uncertainties, along with the larger statistical error on the signal acceptances, are included in deriving the exclusion contours, and are found to be less than 10%. Some of the theoretical uncertainties, such as the effects of rotation,

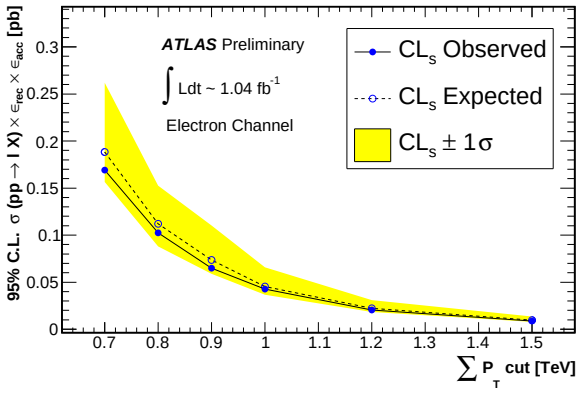

(a) Electron channel

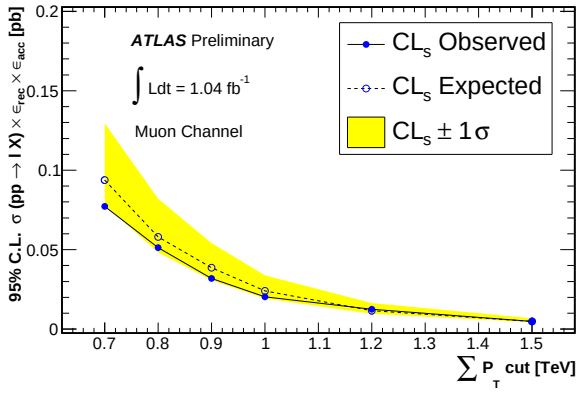

(b) Muon channel

Figure 4: 95% C.L. upper limits on the effective cross section ($\sigma_{\text{eff}} = \sigma(pp \to \ell X) \cdot \epsilon_{\text{rec}} \cdot \epsilon_{\text{acc}}$) as a function of $\sum p_{\text{T}}$ cut. The expected and observed limits according to the CL_s prescription are shown, as well as the 1σ bounds on the expected limit. For the models considered, $\epsilon_{\text{rec}} \cdot \epsilon_{\text{acc}}$ varies, averaging 74% (51%) for the electron (muon) channel. The full range of $\epsilon_{\text{rec}} \cdot \epsilon_{\text{acc}}$ is 60 – 90% for the electron channel and 40 – 60% for the muon channel.

or spin, are discussed in Section 1. One of the more significant theoretical uncertainties is that associated with the decay of the state as its mass approaches M_{D}. Common prescriptions are to assume thermal emissions as the mass falls below M_{D}, all the way down to complete evaporation, or to end thermal emissions at some mass close to M_{D}, at which point the state decays immediately to a remnant state, the multiplicity of which is uncertain. The efficiency of the event selection in analyses could differ significantly according to the remnant model choice, particularly for samples in which a limited number of Hawking emissions are anticipated, motivating the consideration of multiple remnant models.

The 95% exclusion contours in the M_{D}-M_{TH} plane (M_{S}-M_{TH} plane for string balls) for different models are obtained using the CL_s prescription. Figure 5 shows exclusion contours for rotating black hole benchmark models with high- and low-multiplicity remnant decays. Their comparison allows an assessment of the effect of this modelling uncertainty on the analysis, which is inevitably greatest in the regime

of low $M_{\mathrm{TH}}/M_{\mathrm{D}}$. Limits for rotating and non-rotating string ball models are shown in Figure 6[4]. The string ball models illustrated were simulated using a high-multiplicity remnant model.

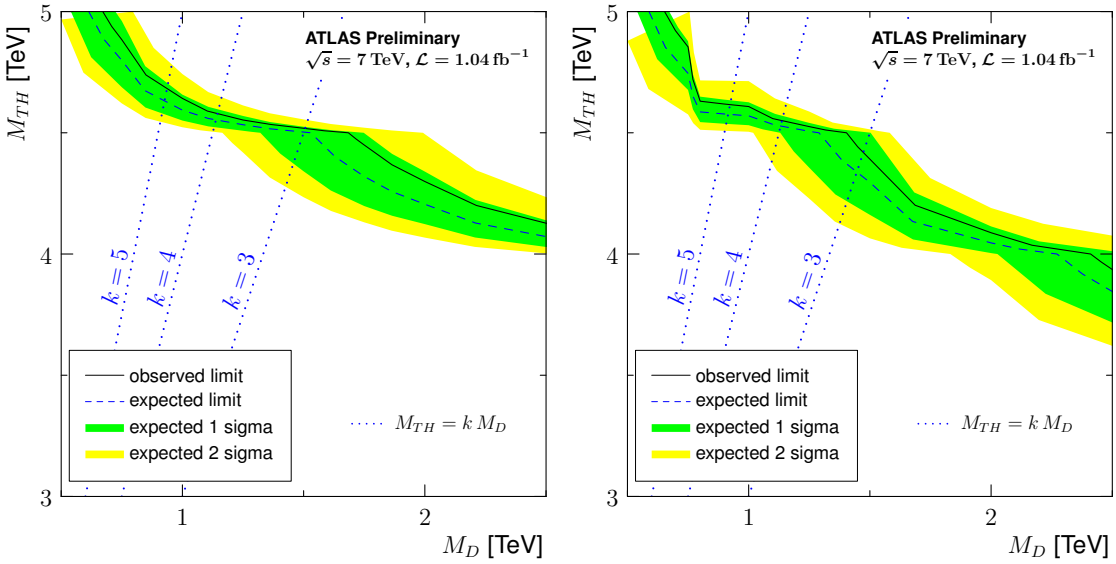

(a) Rotating black holes, with decays ending in a high-multiplicity remnant state, generated with `Blackmax`.

(b) Rotating black holes, with decays ending in a low-multiplicity remnant state, generated with `Charybdis`.

Figure 5: 95% C.L. limit in the M_{TH}-M_{D} plane, both channels combined, for a rotating black hole model with six extra dimensions. The solid (dashed) line shows the observed (expected) limits, with the green and yellow bands the expected 1σ and 2σ variations of the expected limits. The dotted blue lines show lines of constant $k = M_{\mathrm{TH}}/M_{\mathrm{D}}$. The irregularities of the limit contours are caused by the discreteness of the grid samples used and their interpolation into a continuous line.

[4]The narrowing of the limit bands at $M_{\mathrm{S}} \sim 0.75$ TeV is due to the presence of a sample point lying directly on the limit; at other points, a longer interpolation is needed.

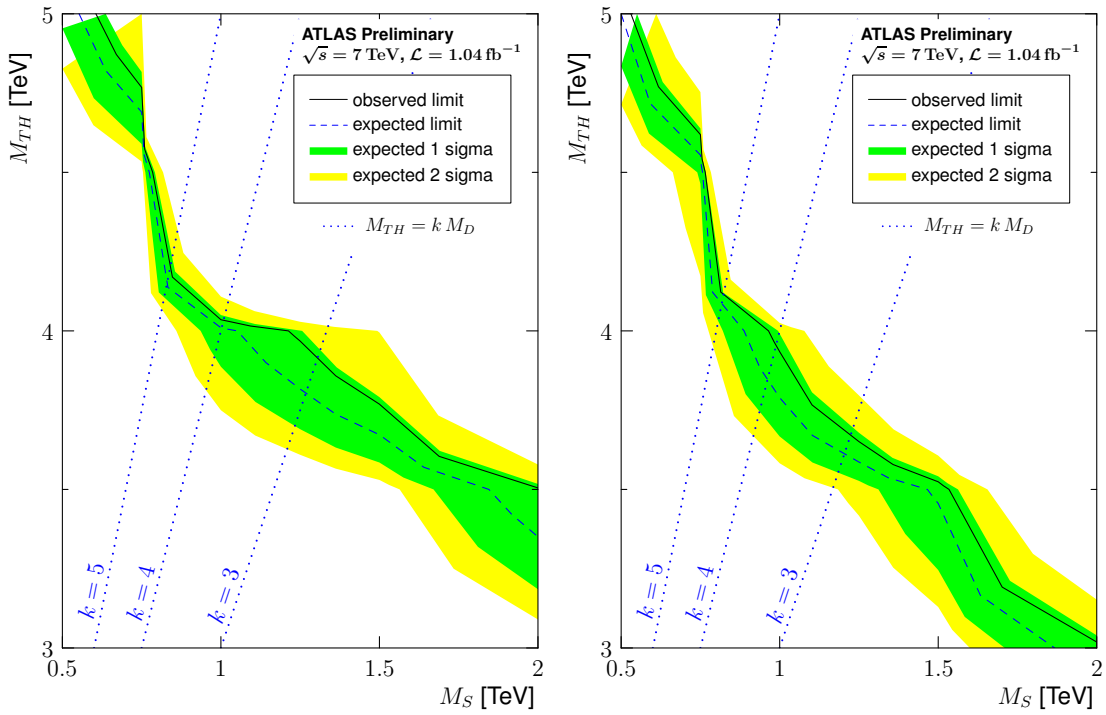

(a) Non-rotating string balls.

(b) Rotating string balls.

Figure 6: 95% C.L. limit in the M_{TH}-M_{D} plane, both channels combined for rotating and non-rotating string balls with six extra dimensions. The solid (dashed) line shows the observed (expected) limits, with the green and yellow bands the expected 1σ and 2σ variations of the expected limits. The dotted blue lines show lines of constant $k = M_{\mathrm{TH}}/M_{\mathrm{D}}$. All samples were produced with the `Charybdis` generator. The irregularities of the limit contours are caused by the discreteness of the grid samples used and their interpolation into a continuous line.

11 Summary

This note presents a search for microscopic black holes and string ball states in ATLAS using a total integrated luminosity of 1.04 fb^{-1}. This search has considered final states with three or more high transverse momentum objects, at least one of which was required to be a lepton (electron or muon). No deviation from the Standard Model was observed in either the electron or the muon channels. Consequently, limits are set on TeV-scale gravity models, interpreted in a two-dimensional parameter grid of benchmark models (the M_{D}-M_{TH} plane). 95% C.L. upper limits are set on the effective cross sections for new physics in these final states: $\sigma_{\mathrm{eff}} = \sigma(pp \to \ell X) \cdot \epsilon_{\mathrm{rec}} \cdot \epsilon_{\mathrm{acc}}$, where $\sigma(pp \to \ell X)$ is the production cross section for a high-$\sum p_{\mathrm{T}}$ multi-object state containing a high-p_{T} (> 100 GeV) isolated lepton inside experimental acceptance. For $\sum p_{\mathrm{T}} > 1.5$ TeV, the upper limits on the cross section are 8.7 fb for the electron channel and 4.8 fb for the muon channel, at 95% C.L.

References

[1] L. Randall and R. Sundrum, Phys. Rev. Lett. **83** (1999) 3370–3373.

[2] N. Arkani-Hamed, S. Dimopoulos, and G. R. Dvali, Phys. Lett. B **429** (1998) 263–272.

[3] I. Antoniadis, N. Arkani-Hamed, S. Dimopoulos, and G. R. Dvali, Phys. Lett. B **436** (1998) 257–263.

[4] LEP Exotica Working Group, the ALEPH, DELPHI, L3 and OPAL Collaborations, CERN Note LEP Exotica WG 2004-03 (2004) .

[5] CDF Collaboration, Phys. Rev. Lett. **101** (2008) 181602.

[6] D0 Collaboration, Phys. Rev. Lett. **101** (2008) 011601.

[7] ATLAS Collaboration. arXiv:1106.5327 (2011) [hep-ex].

[8] CMS Collaboration. arXiv:1106.4775 (2011) [hep-ex].

[9] S. Dimopoulos and R. Emparan, Phys. Lett. B **526** (2002) 393–398.

[10] D. M. Gingrich and K. Martell, Phys. Rev. D. **78** (2008) 115009.

[11] H. G. Luis A. Anchordoqui, Jonathan L. Feng and A. D. Shapere, Phys. Rev. D **65** (2002) 124027.

[12] D. M. Gingrich, Int. J. Mod. Phys. A **21** (2006) 6653–6676.

[13] K. S. Thorn. W.H.Freeman & Co Ltd, San Francisco, 2002. In Magic Without Magic: John Archibald Wheeler.

[14] S. Hawking, Commun. Math. Phys. (1975) .

[15] D. N. Page, Phys. Rev. D **13** (1976) 198.

[16] J. A. Frost et al., JHEP **10** (2009) 014.

[17] ATLAS Collaboration, ATLAS-CONF-2010-088 (2010) .

[18] CMS Collaboration, Physics Letters B **697** (2011) no. 5, 434 – 453.

[19] CMS Collaboration, CMS-PAS-EXO-11-071 (2011) .

[20] ATLAS Collaboration, ATLAS-CONF-2010-068 (2011) .

[21] ATLAS Collaboration, ATLAS-CONF-2010-065 (2011) .

[22] P. Meade and L. Randall, JHEP **05** (2008) 003.

[23] ATLAS Collaboration, New J. Phys. **13** (2011) 053044.

[24] ATLAS Collaboration, JINST **3** (2008) S08003.

[25] ATLAS Collaboration, ATLAS-CONF-2011-116 (2011) .

[26] ATLAS Collaboration, ATLAS-CONF-2011-114 (2011) .

[27] ATLAS Collaboration, ATLAS-CONF-2010-095 (2010) .

[28] T. Sjostrand, S. Mrenna, and P. Z. Skands, JHEP **05** (2006) 026.

[29] A. Sherstnev and R. S. Thorne, Eur. Phys. J. C **55** (2008) 553–575.

[30] S. Frixione and B. R. Webber, JHEP **06** (2002) 029; S. Frixione, P. Nason and B. R. Webber, JHEP **08** (2003) 007; S. Frixione, E. Laenen and P. Motylinski, JHEP **03** (2006) 092 .

[31] P. M. Nadolsky et al., Phys. Rev. D **78** (2008) 013004.

[32] M. L. Mangano, M. Moretti, F. Piccinini, R. Pittau, and A. D. Polosa, JHEP **07** (2003) 001.

[33] J. Pumplin et al., JHEP **07** (2002) 012.

[34] T. Gleisberg et al., JHEP **02** (2004) 056.

[35] G. Corcella et al., JHEP **0101** (2001) 010.

[36] J. Butterworth, J. Forshaw, and M. Seymour, Z. Phys. **C72** (1996) 637–646.

[37] ATLAS Collaboration, ATL-PHYS-PUB-2011-008 (2011) .

[38] S. Agostinelli et al., Nucl. Instr. and Meth. A **506** (2003) 250–303.

[39] ATLAS Collaboration, Eur. Phys. J. C **70** (2010) 823–874.

[40] D.-C. Dai, G. Starkman, D. Stojkovic, C. Issever, E. Rizvi, and J. Tseng, Phys. Rev. D **77** (2008) 076007.

[41] D.-C. Dai, C. Issever, E. Rizvi, G. Starkman, D. Stojkovic, and J. Tseng. arXiv:0902.3577 [hep-ph].

[42] ATLAS Collaboration, JHEP **12** (2010) 060.

[43] ATLAS Collaboration, arXiv:1108.1316 (2011) [hep-ex] .

[44] M. Cacciari, G. P. Salam, and G. Soyez, JHEP **04** (2008) 063.

[45] ATLAS Collaboration, ATL-LARG-PUB-2008-002 (2011) .

[46] ATLAS Collaboration, ATLAS-CONF-2011-032 (2011) .

[47] ATLAS Collaboration, ATLAS-CONF-2010-038 (2010) .

[48] ATLAS Collaboration, Eur. Phys. J. C **71** (2011) 1–36.

[49] ATLAS Collaboration, ATLAS-CONF-2010-054 (2010) .

[50] A. L. Read, J. Phys. G **28** (2002) 2693–2704.